Cascade Flow Calculations by a Multigrid Euler Method

Feng Liu* and Antony Jameson†
Princeton University, Princeton, New Jersey 08544

An explicit finite-volume method for the Euler equations with multigrid is presented for calculating cascade flows. The method is validated against theoretical test cases of the Hobson shock-free impulse cascade and a supersonic wedge cascade. Results for a VKI turbine cascade and a low-pressure turbine cascade are presented and compared with experimental data. Isentropic Mach number distributions on blade surfaces show good agreement with experiments at design conditions, whereas, discrepancy exists at off-design conditions due to flow separation. With equal efficiency the method is also able to capture qualitative features of secondary flow due to inlet side-wall boundary layers.

Nomenclature

c	=	sound speed
D	=	artificial dissipation
E	=	stagnation energy
E, F, G	=	flux vectors in the Euler equations
H	=	stagnation enthalpy
(i, j, k)	=	grid point indices
k	=	summation index
P	=	forcing function in the multigrid method
p	=	pressure
q	=	total flow speed
Q	=	flux balance
R	=	residual for the Euler equations
$\bar{R}$	=	averaged residual for the Euler equations
S	=	entropy
(u, v, w)	=	velocity components in x, y, z directions
V_{ijk}	=	cell volume
W	=	conserved flow variables in the Euler equations
(x, y, z)	=	Cartesian coordinates
(α, β, γ)	=	inlet flow directional angles
α_q	=	time-stepping coefficient for the qth stage of the multistage time-stepping scheme
γ	=	ratio of specific heats
ΔS	=	cell surface area
δ	=	central difference operator, $\delta_x(\cdot) = (\cdot)_{i+1/2} - (\cdot)_{i-1/2}$
ε	=	smoothing parameter
ρ	=	density
Ω	=	control volume

Subscripts

$h, 2h$	=	coarse and fine meshes
i	=	interior cell values
n	=	outer normal direction to a boundary
q	=	stages in the multistage time stepping
∞	=	far-stream conditions

I. Introduction

IN order to take full advantage of computational fluid dynamics in the design of turbomachinery blade rows, it is important to develop numerical methods that offer both accurate solutions for realistic flows and minimum computer cost and turn-around time. While a three-dimensional Navier-Stokes solver is really needed for the above purpose, the problem of turbulence modeling and the large amount of computer time make a fast and robust three-dimensional Euler solver still a desirable tool for routine applications. Furthermore, since the Euler equations do not preclude rotational flow, it is anticipated that, when proper inlet boundary conditions are given and a fine enough mesh is provided, the Euler equations are capable of capturing features of secondary flow vortices caused by the convection of the inlet side-wall boundary layers.

A notable Euler method for cascade-flow calculations was developed by Denton.[1] The robustness, relative fast speed, and simplicity of the method earned its wide use in the turbomachine industry. On the other hand, a finite-volume method with a multiple stage time-stepping scheme proposed by Jameson et al.[2] has been very successful for external flows. This method has the advantage of separated spatial and time discretizations and is easy to implement. Coupled with a multigrid scheme, the method can achieve computational efficiencies better than most other existing methods. Holmes[3] first applied a four-stage version of the method without multigrid to cascade calculations. Smith and Caughey[4] later incorporated multigrid and presented results for a rotor cascade. In this article we will present results with our latest version of a five-stage cell-centered finite-volume method with multigrids. The method is validated against theoretical test cases of the Hobson shockless impulse cascade and a supersonic wedge cascade. Detailed studies are carried out on a three-dimensional turbine cascade and the results are compared with those by Hodson and Dominy.[5–7] One interesting feature of this work is that the method has been applied to calculating rotational flow in an attempt to explore the possibility of predicting cascade secondary flow with an Euler code.

In the next section we will outline the basic numerical method. Section III describes the boundary conditions for typical cascade calculations. Section IV shows the results for the Hobson impulse cascade, a supersonic wedge cascade, and two turbine cascades. Comparisons of blade isentropic Mach number distributions will be made between numerical calculation and experiment. Preliminary results of secondary flow calculations will also be presented to illustrate the capability and limitations of the inviscid calculation.

II. Numerical Method

A. Finite-Volume Scheme and Time Stepping

The basic numerical method is described in detail in Refs. 8 and 9. For a perfect gas

$$E = [p/(\gamma - 1)\rho] + \tfrac{1}{2}(u^2 + v^2 + w^2), \qquad H = E + (p/\rho)$$

The Euler equations can be written in integral form as

$$\frac{\partial}{\partial t} \int_\Omega W \, dV + \oint_{\partial\Omega} [E \, dS_x + F \, dS_y + G \, dS_z] = 0 \quad (1)$$

for a fixed region Ω with boundary $\partial\Omega$, where

$$W = \begin{bmatrix} \rho \\ \rho u \\ \rho v \\ \rho w \\ \rho E \end{bmatrix} \quad E = \begin{bmatrix} \rho u \\ \rho uu + p \\ \rho uv \\ \rho uw \\ \rho uH \end{bmatrix}$$

$$F = \begin{bmatrix} \rho v \\ \rho uv \\ \rho vv + p \\ \rho vw \\ \rho vH \end{bmatrix} \quad G = \begin{bmatrix} \rho w \\ \rho uw \\ \rho vw \\ \rho ww + p \\ \rho wH \end{bmatrix}$$

The computational domain is divided into hexahedral cells. A system of ordinary differential equations can be obtained by applying Eq. (1) to each cell and approximating the surface integral with a finite-volume scheme

$$\frac{d}{dt} (V_{ijk} W_{ijk}) + Q_{ijk} = 0 \quad (2)$$

where W_{ijk} is the average flow variable over the cell, Q_{ijk} is the finite-volume approximation for the net flux out of the cell. With a cell-centered scheme W_{ijk} is assumed to be at the center of the cell. Q_{ijk} can be evaluated as

$$Q_{ijk} = \sum_{k=1}^{6} [E_k(\Delta S_x)_k + F_k(\Delta S_y)_k + G_k(\Delta S_z)_k] \quad (3)$$

Where E_k, F_k, and G_k denote values of the flux vectors E, F, and G on the kth face of the cell, $(\Delta S_x)_k$, $(\Delta S_y)_k$, and $(\Delta S_z)_k$ are the x, y, z components of the face area vector. E_k, F_k, and G_k can be evaluated by taking the averages of E, F, and G, respectively, on either side of the cell face.

The scheme constructed in this manner reduces to a central-difference scheme on Cartesian meshes, and is second-order accurate if the mesh is sufficiently smooth. To prevent odd and even decoupling and to capture shocks without oscillations, an additional dissipation term is added to the semidiscrete Eq. (2) so that we solve

$$\frac{dW_{ijk}}{dt} + R_{ijk}(W) = 0 \quad (4)$$

where R_{ijk} is the residual

$$R_{ijk}(W) = (1/V_{ijk})(Q_{ijk} - D_{ijk})$$

and D_{ijk} is the artificial dissipation term which is formed in a conservative manner as a flux balance of blended first and third differences of the flow variables in each coordinate direction.[8]

Equation (4) is then integrated in time by an explicit multistage scheme. Multistage schemes are chosen because of their extended stability limit and high frequency damping properties which are appropriate for multigrid schemes. For our calculations we have used a five-stage scheme with evaluations of the dissipation term only at the first, third, and fifth stages. The readers are referred to Refs. 8 and 9 for details of the time-stepping scheme. The allowable Courant number for the five-stage scheme is 4.0. This number can be further increased by smoothing the residuals at each stage.

This is done in the following product form in three dimensions:

$$(1 - \varepsilon_x \delta_x^2)(1 - \varepsilon_y \delta_y^2)(1 - \varepsilon_z \delta_z^2) \bar{R}_{ijk} = R_{ijk}$$

Where ε_x, ε_y, and ε_z are the smoothing parameters in each direction. Since it is only necessary to solve a sequence of tridiagonal equations for separate scalar variables, this scheme requires a relatively small amount of computational effort per time step. Coupled with a multigrid scheme, the five-stage time-stepping scheme with residual smoothing shows excellent convergence rate. Although diagonalized fully implicit methods are also available,[10] the simplicity and applicability of the method of residual smoothing for use on unstructured grids[11] and parallel computing make it a desirable alternative.[12]

It can be shown for a one-dimensional model problem without dissipation that the scheme can be made stable for any Courant number, provided the smoothing parameter is large enough.[8] In our calculation, best convergence is achieved at Courant numbers around nine with minimum smoothing. In order to further increase the rate of convergence, locally varying time steps and enthalpy damping can also be used. Both of these techniques are based on the assumption that the solution approaches a steady state, and thus will not work for time-accurate solutions.[8,9]

B. Multigrid Method

The most effective method of accelerating convergence is the multigrid method. Auxiliary meshes are introduced by doubling the mesh spacing, and values of the flow variables are transferred to a coarser grid by the rule

$$W_{2h}^{(0)} = \sum V_h W_h / V_{2h}$$

where the subscripts denote values of the mesh spacing parameter. In three dimensions the sum is over the eight cells on the fine grid composing each cell on the coarse grid. The rule conserves mass, momentum, and energy. A forcing term is then defined as

$$P_{2h} = \sum R_h(W_h) - R_{2h}(W_{2h}^{(0)})$$

where R is the residual of the difference scheme. To update the solution on a coarse grid the multistage scheme is reformulated as

$$W^{(1)} = W_{2h}^{(0)} - \alpha_1 \Delta t (R_{2h}^{(0)} + P_{2h})$$
$$\cdots$$
$$W^{(q+1)} = W_{2h}^{(0)} - \alpha_{q+1} \Delta t (R_{2h}^{(q)} + P_{2h}) \quad (5)$$
$$\cdots$$

where $R^{(q)}$ is the residual of the qth stage. In the first stage of the scheme, the addition of P_{2h} cancels $R_{2h}[W_{2h}^{(0)}]$ and replaces it by $\sum R_h(W_h)$, with the result that the evolution on the coarse grid is driven by the residual on the fine grid. This process is repeated on successively coarser grids. Finally the correction calculated on each grid is passed back to the next finer grid by bilinear interpolation. In the present implementation a W-cycle strategy[12] is used in each time step.

Since the evolution on a coarse grid is driven by residuals collected from the next finer grid, the final solution on the fine grid is independent of the choice of dissipation and boundary conditions on the coarse grids when the computation converges. To reduce the computational effort, only first-difference dissipation is used on the coarse grids. For external flow calculations, some further reduction of computational effort can be achieved by freezing the far-field boundary conditions on the coarse grid calculations. It was found that, due to the strong interactions of the inflow and outflow boundary conditions with the interior flow in a cascade blade row, slow convergence and possible limit cycles may be encountered if the inflow and outflow boundary conditions are not updated

on each multigrid level as well as on the fine grid. In the current work, the same boundary conditions discussed in the next section are applied to all boundaries on all levels of the grids.

III.   Boundary Conditions

At present, H-type meshes are used. For cascade calculations we usually encounter four types of boundaries: 1) wall, 2) periodic, 3) inlet, and 4) outlet as shown in Fig. 1. Implementation of boundary conditions for a cell-centered finite-volume scheme is usually facilitated by using fictitious cells exterior to the boundaries of the computational domain. For wall boundaries, zero normal velocity is imposed, and we use the normal momentum equation to extrapolate the pressure to the wall. For periodic boundaries, e.g., ab and AB in Fig. 1, the flow variables in the fictitious cells below AB are made to be the same as those in the interior cells right below ab, and the flow variables in the fictitious cells above ab are made to be the same as those right above AB. Since a cell-centered scheme is used, no special treatment is needed for the leading and trailing edges of the blade profile.

At the inlet boundary, four of the five independent flow variables must be specified for subsonic inlet flow. The other flow variable must be extrapolated from inside the flowfield according to characteristic analysis. For external flows, the far-stream velocity is known since it is simply determined by the flight speed. Therefore, we may specify a known velocity component and let the flow angle be determined by the computation which should approach the undisturbed freestream condition if the boundary is far enough from the airfoil or wing. For cascade flows, usually the total pressure and total temperature (enthalpy) are given upstream. The velocity magnitude at the inlet, however, is determined by the back pressure downstream of the cascade. Different back pressures result in different velocities at the inlet. The flow angle, on the other hand, does not change much even when the velocity magnitude changes. In an experimental setup, e.g., the flow upstream comes from a stabilizing chamber where the flow is conditioned to be a nearly parallel stream entering the cascade at a specific incidence angle. Specification of a velocity component is not a rational choice without knowing at least approximately what the velocity magnitude is. If a rather arbitrary velocity component not consistent with the back pressure is chosen for the inlet, the resulting flowfield will then have a quite different incidence angle from the experimental condition. In light of the above argument we choose to specify the total enthalpy, entropy, which is equivalent to total pressure, and the two independent flow angles of the incoming

flow. The one-dimensional Riemann invariant normal to the flow boundary is used to obtain the other condition. Let q_n be the velocity component in the direction of the outer normal of the inlet boundary and c the speed of sound for the fictitious cells outside the inlet boundary, and let subscript i denote the corresponding values on the interior cells adjacent to the inlet boundary. The outgoing one-dimensional characteristic equation can be written as

$$q_{n,i} + [2/(\gamma - 1)]c_i = q_n + [2/(\gamma - 1)]c \qquad (6)$$

The conditions for the entropy, enthalpy, and flow angles can be written as

$$S = S_\infty \qquad (7)$$

$$H = H_\infty \qquad (8)$$

$$(u/q) = \cos \alpha, \quad (v/q) = \cos \beta, \quad (w/q) = \cos \gamma \qquad (9)$$

where S_∞, H_∞, α, β, and γ are the given entropy, total enthalpy, and the flow angles. α, β, and γ satisfy the following condition:

$$\cos \alpha^2 + \cos \beta^2 + \cos \gamma^2 = 1 \qquad (10)$$

With the above equations we can solve for all the flow variables on the boundary, or rather, with the cell-centered scheme flow variables on the fictitious cells adjacent to the boundary. For supersonic inlet flow, all flow variables are specified.

Conversely on the outlet boundary, entropy, total enthalpy or the outgoing one-dimensional Riemann invariant, and flow angles are extrapolated for subsonic flow. In principle, an upstream running characteristic has to be used to reflect the fact of upstream influence in subsonic flows. However, in view of experimental setup where the back pressure is controlled by a throttling device, here we choose to directly specify the pressure at the exit of the cascade. For outlet flow with supersonic axial velocity all variables are extrapolated.

Because of the existence of the hub and casing in a three-dimensional cascade, the flow develops boundary layers over the sidewalls before it enters the cascade blading where low-energy flow in the sidewall boundary layers undergoes the same blade-to-blade pressure gradient as the inviscid core flow. The interaction of these sidewall boundary layers with the cascade blades results in secondary flow phenomena. It appears that the essential vortical features of secondary flows may be determined by inviscid vortex dynamics which can be described by the Euler equations provided a rotational velocity profile that include the sidewall boundary layers is specified at the entrance of the cascade. This velocity profile can be taken from experimental measurement or obtained by assuming appropriate boundary-layer profiles with given momentum and displacement thicknesses. The velocity profile is then converted into an entropy or stagnation pressure profile by assuming a constant static pressure at the inlet boundary, and with a given stagnation enthalpy so that implementation of the inlet boundary conditions can be carried out in the manner described in the above paragraphs. It must be pointed out, however, that secondary flows are really of viscous origin, and therefore, the results of inviscid simulation ought to be appropriately interpreted.

IV.   Computational Results

A.   Hobson's Impulse Cascade

One of the most difficult test cases for transonic cascade calculations is the Hobson shock-free impulse cascade.[13] It has very thick airfoils and was designed with the hodograph method to give a shock-free supersonic pocket. Since any such shock-free solution is isolated in the sense that a small perturbation in the flow conditions or airfoil shape can cause a
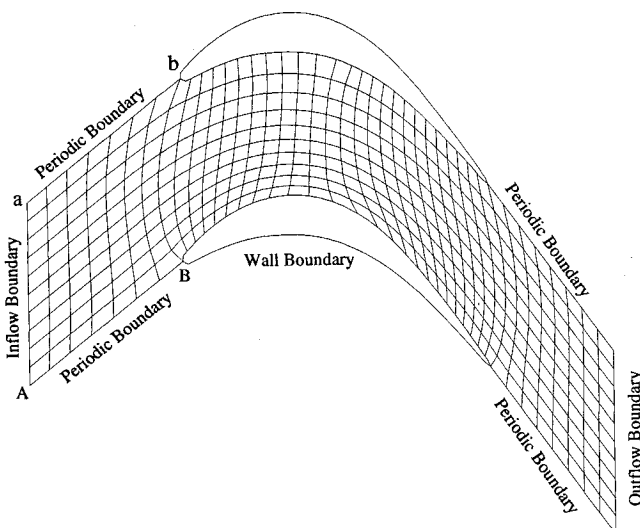

Fig. 1   Computational domain and boundaries for typical cascades with an H grid.

shock wave to occur, Hobson's cascade provides a difficult test of both the accuracy and convergence for a method. Ives calculated the flow of this cascade by a potential flow method.[14] The result, however, showed a noticeable shock terminating the supersonic pocket in both the C_p distribution and the Mach number contour plots. Figure 2 shows the C_p distribution obtained by the present method with an 80 × 24 mesh. Forty-eight points are distributed on the upper and lower surfaces each. It can be seen that the solution is essentially shock free and in close agreement with the original hodograph design. Figure 3 shows the Mach number contours of the same solution. Because this cascade is shock-free and geometrically symmetric before and after in the streamwise direction, the flowfield should be symmetric likewise. If for any reason a shock is present in the passage, then the flowfield would no longer be symmetric. The smooth symmetric pattern shown in Fig. 3 is an indication of the accuracy of the solution.

B. Supersonic Wedge Cascade

Denton presented a supersonic wedge cascade in Ref. 1 as a test case for capturing oblique shocks in cascades. Figure 4 shows the profile of the cascade and the pressure contours of a solution with inlet Mach number 2 calculated by the present
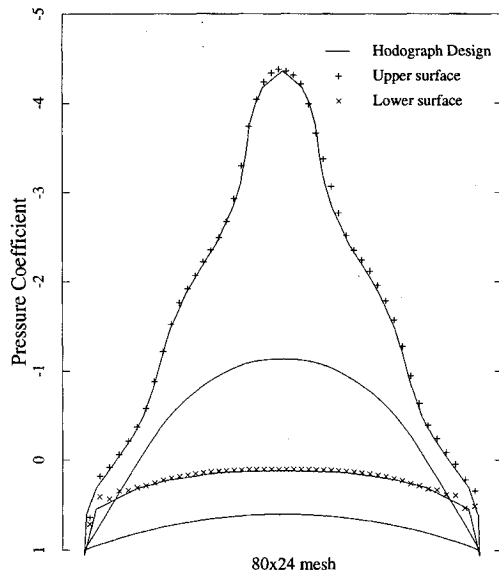

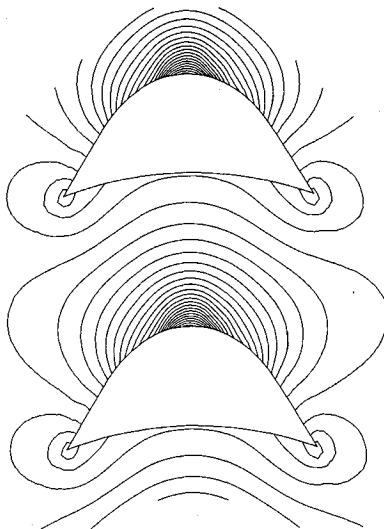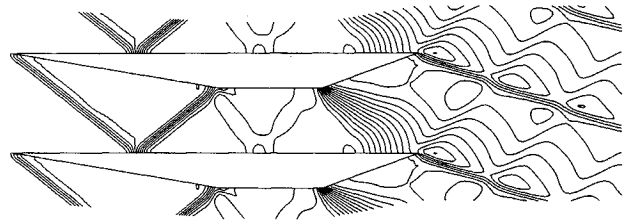Fig. 4   Profile and pressure contour of supersonic wedge cascade.
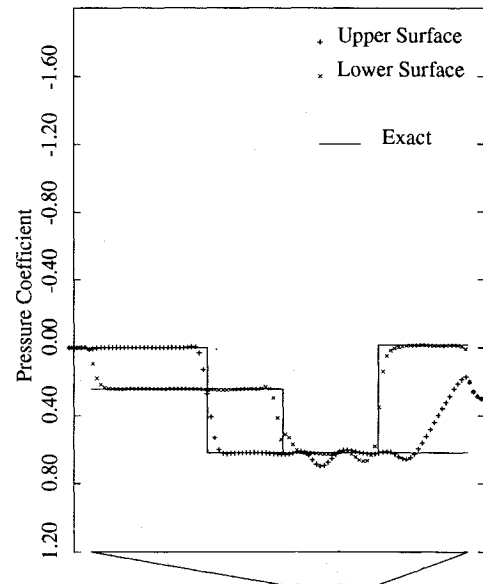
Fig. 5   Surface pressure distribution over supersonic wedge cascade.

Fig. 2   Profile and pressure coefficient distribution over Hobson cascade.

Fig. 3   Mach number contour of Hobson cascade.

method. The shock reflected from the lower blade is designed to be exactly cancelled out at the corner of the upper blade, giving a uniform flow between the parallel surfaces and an expansion off the downstream corner. This design gives a good test case for numerical methods, since the inevitable smearing of shock fronts in a shock-capturing method and any possible wrong prediction of shock angle prevent complete cancellation of the reflected shock, and thus produce a nonuniform region downstream. Figure 5 shows the pressure distribution on the blade obtained by the present method. Comparison of our results and those by Denton[1] shows that the solution of the present method has a more uniform flow region after the reflected shock. This is an indication of better resolution of the shock waves. However, the reflected shock is still not completely cancelled out by the corner of the upper blade. This causes oscillations in both the pressure and Mach number distributions as shown in Figs. 5 and 6. In addition, the Mach number in the expansion region is lower than that of the analytic solution, although the pressure has fully recovered to the analytic value as shown in Fig. 5. This is an indication of entropy production and is caused by the large dissipation incurred at the corner point where the flowfield has a sharp discontinuity due to the expansion waves. As pointed out, a complete cancellation may never be achieved by a shock-capturing method due to the finite thickness of the shock waves. Improvements, however, may be expected for such flows by using solution-adaptive grids with more grid points clustered near the shocks, or more sophisticated schemes of higher shock resolution, such as the TVD or other upwinding-type schemes.

C. VKI Turbine Cascade

This is a two-dimensional turbine nozzle cascade.[15] Both the two-dimensional and three-dimensional programs are used to calculate the flow through this cascade. The three-dimensional results with uniform inlet flow are found to be identical
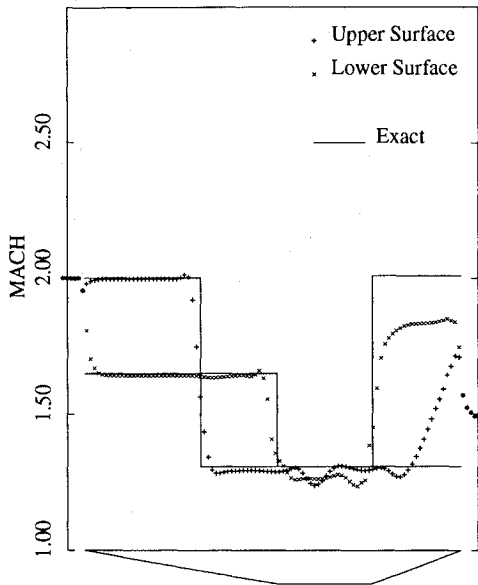
Fig. 6 Surface Mach number distribution over supersonic wedge cascade.
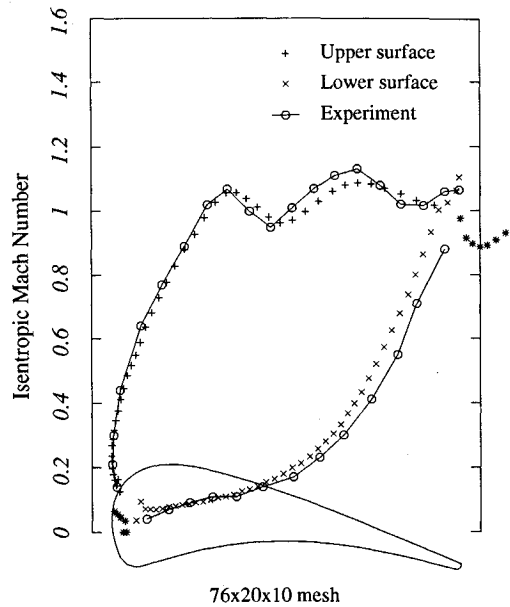

76x20x10 mesh

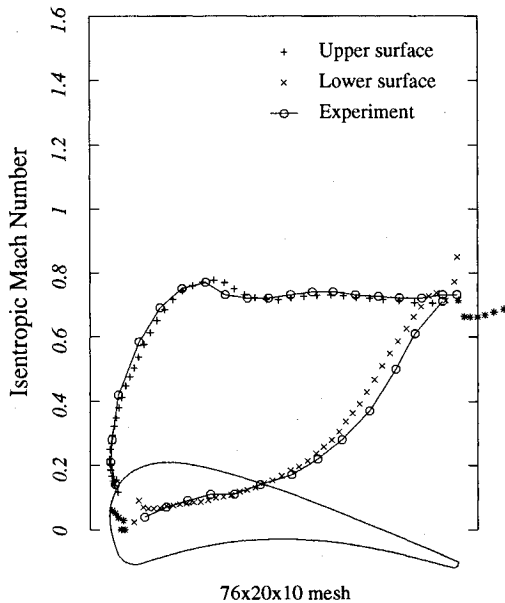**Fig. 7 Isentropic Mach number distribution over VKI cascade at exit isentropic Mach 0.7.**

76x20x10 mesh

Fig. 8 Isentropic Mach number distribution over VKI cascade at exit isentropic Mach 1.0.

76x20x10 mesh, 2 level(s) of multigrid W-Cycle

Fig. 9 Convergence history for VKI cascade at exit isentropic Mach 1.0.

to our two-dimensional solution as they should be. A 77 × 21 H-mesh with the same surface definition as proposed in Ref. 15 was used in the blade-to-blade plane. The interior points of the mesh are redistributed by an elliptic mesh generator after Thompson et al.[16] A three-dimensional mesh is constructed by stacking these two-dimensional H-meshes in the spanwise direction, forming a three-dimensional linear cascade with straight side walls. The aspect ratio of the blade is 0.4. Because of the small aspect ratio, only 11 grid points are used in the spanwise direction.

Figure 7 shows the blade surface isentropic Mach number distributions of both experiment[15] and our calculation for an isentropic exit Mach number 0.7. The comparison shows good agreement except at the trailing edge of the blade where the numerical solution shows two points with large suction. This is probably due to the fact that we did not use any cusp to modify the round trailing edge of the blade profile. Figure 8 shows the solution of the same cascade at exit isentropic Mach number 1.0. Good agreement with experimental data is also obtained. The fast convergence to be shown below, and the
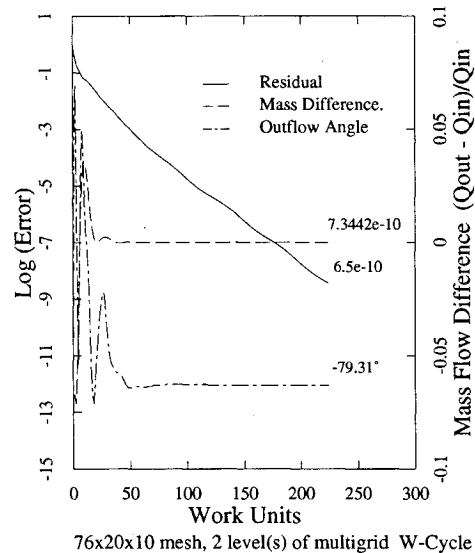
good agreement with experimental data without adding a cusp, demonstrate the robustness of the scheme.

Figure 9 plots the convergence history for the transonic calculation at exit isentropic Mach number 1.0. The computation was done with two levels of multigrids. For three-dimensional calculations, the number of grid points on the coarse grid is $\frac{1}{8}$ of that on the fine grid. Measured by a "work unit" consisting of the computational effort of one time step on the fine grid, the work required for one multigrid cycle with two levels is $1 + \frac{1}{8}$ plus the work required for additional residual calculations and data transfer, which is of the order of 25%. Figure 9 shows that within 200 multigrid time steps, or 225 work units, the residual (shown by the solid line) is driven to the order of 10^{-10}. The dashed line shows the relative difference between the mass flow at the exit and that at the entrance of the cascade. With this difference driven to the order of 10^{-10} we can be sure that our calculation properly conserves mass flow in the cascade passage, which is an important property for internal flow calculations. Such a calculation on the 77 × 21 × 11 mesh with 200 multigrid time steps takes a total of 840 s on a single processor of a Convex

C2 computer in double precision. Double precision was used only to show that the scheme is capable of driving the residual beyond the order of 10^{-7}. For engineering applications, the residual need only be reduced to the order of 10^{-4}. Figure 9 shows that this can be achieved within a few more than 50 time steps. At that time, the mass flow difference and the outflow angle also show that the solution has effectively reached a steady state.

Since the Euler equations are capable of describing rotational flow, one expects that they can be used to solve flowfields that involve inviscid vortex transport. In cascade problems, secondary flow is not only important for the performance of turbomachines, but also interesting, because there has been the suggestion that certain features of the secondary flow are due to the inviscid convection of the vortices developed on the side walls at the entrance. The Euler equations should be able to predict these features of the secondary flow when given the initial boundary-layer type velocity distribution. The origin of this velocity distribution is, of course, due to viscosity. However, the later development of the vortex flow and its effect on the global flowfield, such as the appearance of passage vortices, may be largely an inviscid process. To demonstrate this idea, we solved the Euler equations for the VKI cascade with a typical inlet boundary-layer velocity distribution. Twenty-one grid points are used in the spanwise direction for this calculation. They are distributed in such a way that the grid has a better resolution near the end-walls to capture the boundary-layer type velocity profile.

Figure 10 shows the swirl in two cross sections of the cascade flowfield. The swirl is defined to be the dot product of the vorticity and velocity vectors normalized by the magnitude of the velocity. Therefore, it is essentially the streamwise vorticity and can be used as a good indication of secondary flow. Cross section A-A cuts through the two counter-rotating horseshoe vortices generated in front of the leading edge as a consequence of the interaction of the side-wall boundary layers and the blade. Each of the horseshoe vortices branch into two legs downstream on either side of the blade. The branches on the pressure side, however, have the same sense of rotation as the passage vortices generated by the pressure gradient between the upper and lower blades, and therefore, cannot be distinguished from the larger passage vortices. The
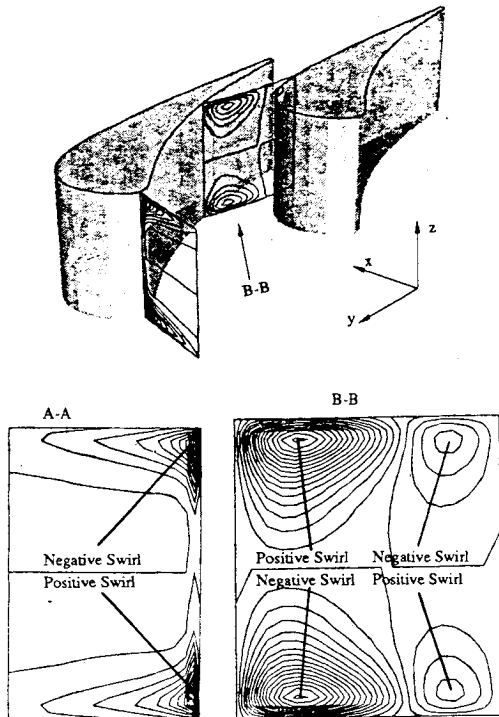
suction side branch of the horseshoe vortices have the opposite sense of rotation and can still be seen downstream in cross section B-B.

D. Low-Pressure Turbine Cascade

This is a turbine cascade with blade profile typical of the root section of a low-pressure aircraft gas turbine. Its side walls have a 6-deg divergence in the blade passage. The cascade has been extensively tested and analyzed by Hodson and Dominy.[5-7] At its design condition this cascade has an exit isentropic Mach number of 0.7 and an incidence angle of 38.8 deg. We calculated this case with a $80 \times 16 \times 16$ mesh. Figure 11 is the typical convergence history for our calculations with three levels of multigrid. Figure 12 shows the is-
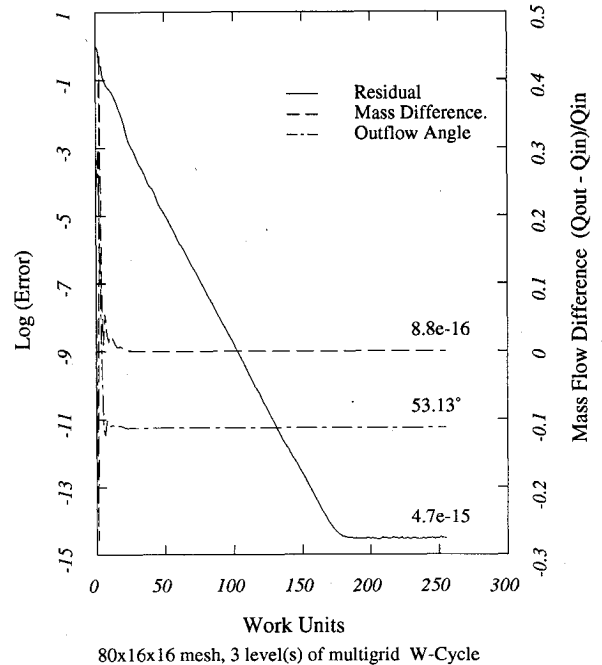

Fig. 11 Convergence history for a low pressure turbine cascade at design condition.

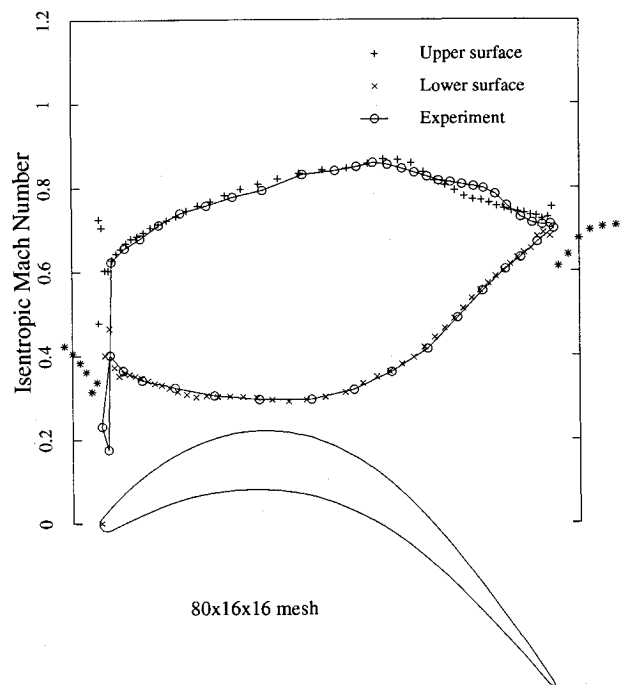Fig. 10 Contours of swirl of VKI cascade in two cross-sectional planes.

Fig. 12 Midspan isentropic Mach number distribution at design condition over a low pressure turbine cascade.

entropic Mach number distribution at midspan, together with the experimental data taken from Ref. 6. It is pointed out in Ref. 6 that there is a separation bubble at about 0.8 chord on the upper surface of the blade. This seems to explain the slight discrepancy between the experimental data and our inviscid solution. The inviscid solution gives a greater adverse pressure gradient than the real viscous flow. The viscous flow cannot sustain the large adverse pressure, and thus separates, changing the outer inviscid flow.

Notice that our solution also predicts a suction peak near the leading edge. This suction peak is followed by a sharp diffusion, and therefore, is likely to cause separation too. Although the experimental data do not show this suction peak, Hodson[5] observed a small separation bubble near the leading edge. In fact, at a larger incidence angle this suction peak becomes obvious in the measured data too. Figure 13 shows the computed and measured isentropic Mach number distribution at an 8.6-deg positive incidence angle relative to the design condition. The measured data is taken from Ref. 7. We can see that the leading-edge suction peak on the upper surface is increased, while that on the lower surface disappears. Overall agreement between experiment and computation is still obtained.

Figure 14 shows another off-design condition with a 20.3-deg negative incidence angle relative to the design angle. We see that in this case there is a large discrepancy between calculation and experiment on the lower blade surface. At 20.3-deg negative incidence angle, there is a long separation bubble on the lower surface after the leading edge as observed by Hodson.[7] The extreme diffusion in that region predicted by the inviscid solution is in fact a good signal of the existence of separation.

For many turbine cascade blades the blade profile often has a blunt trailing edge. Viscous effects dominate in this region, and the Navier-Stokes equations with many grid points have to be used in order to realistically resolve the flow. With an inviscid model, however, the flow will experience a large suction before it reaches a stagnation point because of the high curvature of the blunt trailing edge. The large flow gradient causes lower accuracy and sometimes difficulties in convergence. Many researchers added artificial cusps to avoid this problem. It was mentioned in the last section that our method is tolerant to such blunt trailing edges. Excellent convergence rate was obtained without adding any cusps. However, we did notice in Figs. 7 and 8 the abnormal suction
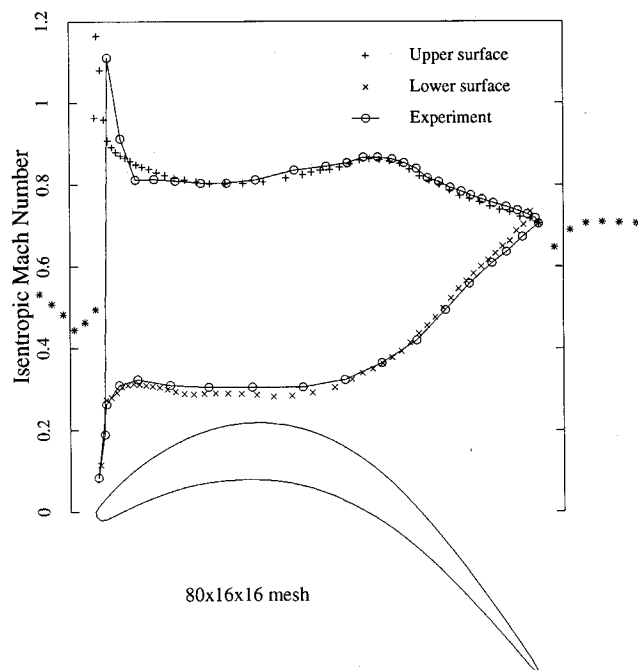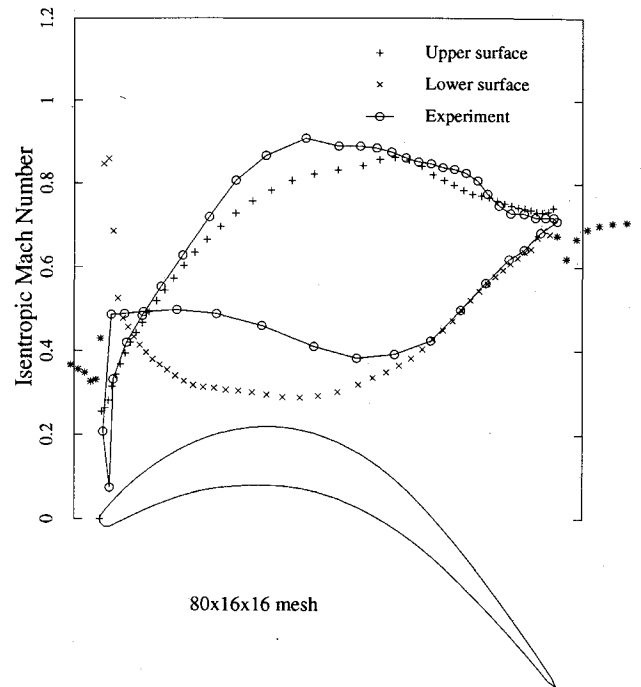

Fig. 14   Midspan isentropic Mach number distribution at − 20.3-deg relative incidence angle off-design condition.

points at the trailing edge. In an effort to remove the abnormal suction, use of cusps were experimented. Because the addition of a cusp usually results in an extended sharp trailing edge, the position of the tip of the trailing edge is important in determining the Kutta condition. We find that a well-chosen rigid cusp for the design condition may not be good at all for off-design conditions. In fact, it may lead to a rather erroneous load for the off-design conditions compared to the experimental data, implying that the Kutta condition is not properly satisfied. To avoid this situation, the results presented in this section at both design and off-design conditions were obtained with a sharpened trailing edge without moving the trailing-edge tip location, rather than with an extended cusp. This seems to give the right overall load on the blade for all flow conditions and reduced suction at the trailing edge.

To simulate secondary flow in this cascade we used the end-wall velocity profile measured by Hodson to obtain the entropy profile at the entrance. In terms of isentropic Mach number distribution at midspan, there is in fact not much difference between the solution of uniform inlet flow and that of a boundary-layer inlet flow. This difference, of course, becomes significant near the end walls. Figure 15 is the span-wise variation of pitchwise mixed-out flow angle. We can see a great overturning of the flow near the end walls due to the low speed in the "boundary layer." This overturning is then followed by an underturning some distance into the flowfield. This is due to the velocity induced by the horseshoe vortex convected downstream from the leading edge. Notice that the underturning cannot be adequately captured if a coarse grid is used. The solutions seem to have converged only after 48 grid cells are used along the blade span. They approach each other on the 160 × 32 × 48 and 160 × 32 × 64 grids as shown in Fig. 15. The peak value of underturning of the converged solution is close to Hodson's experimental data. More grid points along the span are needed for this case than for the VKI cascade because this cascade blade has an aspect ratio of 1.93 which is much larger than that assumed for the VKI cascade. Even on this fine mesh with an inlet boundary layer, the convergence rate remains fast. The average residual is reduced to the order of 10^{-10} after 100 time steps with four levels of multigrid. It can be seen, however, that the position of our peak is displaced toward the end walls. This shift of peak position may be at least partly explained by the fact that a real viscous boundary layer grows in thickness, whereas our fictitious inviscid one does not. The growth of the real bound-
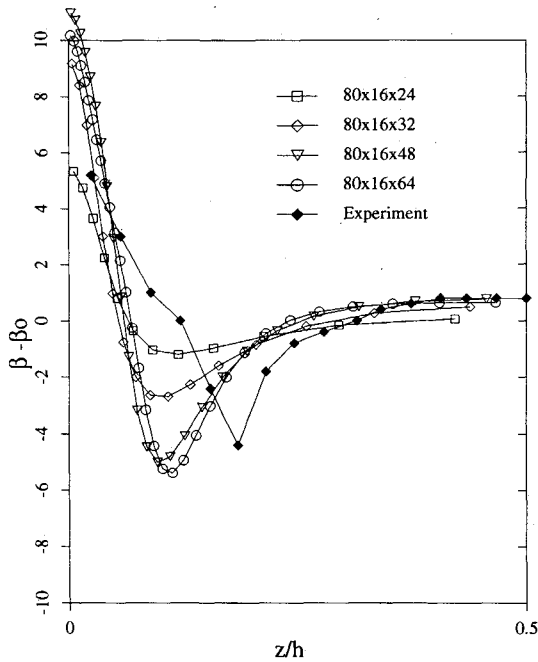

Fig. 13   Midspan isentropic Mach number distribution at + 8.6-deg relative incidence angle off-design condition.

Fig. 15 Spanwise distribution of pitchwise-mixed exit flow angle at 140% axial chord.
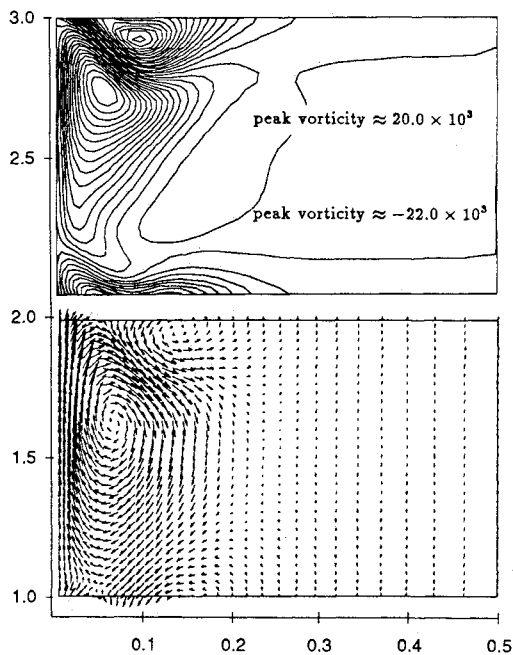

Fig. 16 Secondary velocity vectors and vorticity contours at 140% axial chord.

ary layer will displace the fluid away from the wall, and therefore, cause the vortex to be pushed further inside.

Figure 16 shows the secondary velocity vector field and the vortex contours at 140% Cx. The secondary velocities were obtained by projecting the velocity vectors onto the plane perpendicular to the mixed-out flow direction at the section. The vorticity is then calculated on that plane and plotted with plot3d (the flow visualization package from NASA AMES). Comparison with that obtained by Hodson[6] from an experiment shows that although the positions of the vortices do not agree very well with experiments, the computational results predict qualitatively the same vortex structure.

V. Concluding Remarks

A multigrid finite-volume method for the Euler equations has been developed for calculating two- and three-dimensional cascade flows, including flows with end-wall boundary-layer velocity profiles. An explicit multistage time-stepping scheme is used. The stability limit of the explicit scheme is extended by using implicit residual averaging. Convergence is accelerated by using local time stepping, enthalpy damping, and most of all a multigrid method. The method has been used to calculate the flow through Hobson's shock-free impulse cascade, a supersonic wedge cascade, the VKI turbine nozzle, and a low-pressure turbine cascade with end-wall boundary-layer profiles. Good convergence and overall accuracy can be obtained for blades with blunt trailing edges without adding a cusp. Reduction of residuals in the order of four orders of magnitude is achieved generally within 50–100 times steps. Comparisons with experiments show good accuracy of the method at design conditions. At off-design conditions, however, large separation bubbles may exist and a Navier-Stokes solver must be used. Qualitative results support the idea that the Euler equations are capable of capturing the secondary flow vortices which develop as a consequence of inviscid convection of the entrance velocity profile. Quantitative prediction of secondary flows with an Euler method, however, need be cautioned.

References

[1]Denton, J. D., "An Improved Time Marching Method for Turbomachinery Flow Calculation," *Journal of Engineering for Gas Turbines and Power*, Vol. 105, July 1983, pp. 514–521.
[2]Jameson, A., Schmidt, W., and Turkel, E., "Numerical Solution of the Euler Equations by Finite Volume Methods Using Runge-Kutta Time Stepping Schemes," AIAA Paper 81-1259, June 1981.
[3]Holmes, D. G., and Tong, S. S. "A Three-Dimensional Euler Solver for Turbomachinery Blade Rows," *Journal of Engineering for Gas Turbines and Power*, Vol. 107, April 1985, pp. 258–264.
[4]Smith, W. A., and Caughey, D. A., "Multigrid Solution of Inviscid Transonic Flow Through Rotating Blade Passages," AIAA Paper 87-0608, Jan. 1987.
[5]Hodson, H. P., and Dominy, R. G., "Boundary Layer Transition and Separation Observed Near the Leading Edge of a High Speed Turbine Blade," *Journal of Engineering for Gas Turbines and Power*, Vol. 107, Jan. 1985, pp. 127–134.
[6]Hodson, H. P., and Dominy, R. G., "Three-Dimensional Flow in a Low Pressure Turbine Cascade at its Design Condition," American Society of Mechanical Engineers Paper 86-GT-106, June 1986.
[7]Hodson, H. P., and Dominy, R. G., "The Off-Design Performance of a Low Pressure Turbine Cascade," American Society of Mechanical Engineers Paper 86-GT-188, June 1986.
[8]Jameson, A., *Transonic Flow Calculations*, MAE Rept. 1651, Princeton Univ., Princeton, NJ, July 1983.
[9]Liu, F., "Numerical Calculation of Turbomachinery Cascade Flows," Ph.D. Dissertation, Princeton Univ., Princeton, NJ, June 1991.
[10]Pulliam, T. H., and Steger, J. L., "Recent Improvements in Efficiency, Accuracy and Convergence for Implicit Approximate Factorization Algorithms," AIAA Paper 85-0360, Jan. 1985.
[11]Mavriplis, D. J., and Jameson, A., "Multigrid Solution of the 2D Euler Equations on Unstructured Triangular Meshes," AIAA Paper 87-0353, Jan. 1987.
[12]Jameson, A., "Successes and Challenges in Computational Aerodynamics," AIAA Paper 87-1184, June 1987.
[13]Hobson, D. E., "Shock-Free Transonic Flow in Turbomachinery Cascades," Univ. of Cambridge, Dept. of Engineering Rept. CUED/A Turbo/TR 65, Cambridge, England, UK, 1974.
[14]Ives, D. C., and Liutermoza, J. F., "Second-Order-Accurate Calculation of Transonic Flow over Turbomachinery Cascades," *AIAA Journal*, Vol. 17, No. 8, 1979, p. 870–876.
[15]Sieverding, C., "Test Case 1: 2-D Transonic Turbine Nozzle Blade," *Numerical Methods for Flows in Turbomachinery Blading*, von Karman Inst. for Fluid Dynamics Lecture Series 1982-05, Rhode Saint Genese, Belgium, April 26–30, 1982.
[16]Thompson, J. F., Thames, F. C., and Mastin, C. W., "Automatic Numerical Generation of Body-Fitted Curvilinear Coordinate Systems for Fields Containing Any Number of Arbitrary Two-Dimensional Bodies," *Journal of Computational Physics*, Vol. 15, July 1974, pp. 299–319.